Comparison Between Two Attenuation Models and Precipitation Evaluation With Ground Validation

Denis Alexander Poffo, Jorge Nicolás Saffe, Giorgio Mario Caranti, Raúl Alberto Comess, and Andres Rodriguez, *Member, IEEE*

***Abstract*—In this paper, we present an algorithm to correct the horizontal reflectivity factor Z_h for attenuation by absorption plus scattering of a polarimetric radar located at the Experimental Station of INTA, in Oro Verde, Entre Rios, Argentina. Data correspond to two storms which occurred on November 18, 2009. The correction obtained was compared with models from the literature. Results show good agreement for regions with reflectivity factor lower than 55 dBZ while for regions that go over this limit, the corrections are different. Comparisons with rain gauges indicate the need of more statistics to improve the correlation.**

***Index Terms*—Atmospheric propagation, attenuation, clouds, radar polarimetry, rainfall effects.**

I. Introduction

THE work by Marshall and Palmer [1] greatly contributed to make radar a significant tool for quantitative precipitation estimation. They showed that the size distribution $N(D)$ could be expressed by a simple function of the precipitation intensity, and this implied the existence of a relation between the reflectivity factor Z ($\mathrm{mm}^6/\mathrm{m}^3$) and the precipitation rate R (mm/h).

Further studies (e.g., [2]), showed that there are variabilities from place to place and from storm to storm, making it difficult to establish a unique relation between R and Z. It was suggested that Z may not be enough to provide all the information needed for the quantification of R [3].

The introduction of polarimetric radar paved the way for better relations to estimate R. These radars provide new parameters such as the specific phase difference (KDP) and the differential reflectivity (ZDR). Large (millimetric) raindrops deform as their fall resemble oblate spheroids (with the short axis oriented vertically on average). Therefore, the macroscopic effective (air plus particles) propagation medium possesses an anisotropic refraction index, which causes a difference in optical paths for both the horizontal polarization and the orthogonal one. As a result there will be an increasing phase difference between the two waves as they advance. A different parameter ZDR consists of the ratio between the backscattered intensities of both waves. Consequently a measurement of ZDR provides an estimation of the size of raindrops [4].

In this paper, we present an algorithm to correct the radar reflectivity factor for attenuation using microphysical considerations and data from a disdrometer. These results were used to estimate the precipitation rate which was then compared with rain gauges from four stations. To validate quality of our data it was considered important to compare the present results with procedures by Gu *et al.*, who use polarimetric variables, in particular phase shift ϕ_{DP} which is inmune to attenuation and ρ_{hv} [5].

Manuscript received March 8, 2016; revised May 31, 2016, August 18, 2016, and October 18, 2016; accepted November 17, 2016. Date of publication January 18, 2017; date of current version January 23, 2017. *(Corresponding author: Denis Alexander Poffo.)*

D. A. Poffo, G. M. Caranti, and R. A. Comes are with the Facultad de Matemática, Astronomía y Física, Universidad Nacional de Córdoba, Córdoba 5000, Argentina (e-mail: poffo@famaf.unc.edu.ar; caranti@gmail.com; comes@famaf.unc.edu.ar).

J. N. Saffe and A. Rodriguez are with the Facultad de Ciencias Exactas Físicas y Naturales, Universidad Nacional de Córdoba, Córdoba 5000, Argentina (e-mail: jorgesaffe@gmail.com; androdminplan@gmail.com).

Color versions of one or more of the figures in this paper are available online at http://ieeexplore.ieee.org.

Digital Object Identifier 10.1109/JSTARS.2016.2635807

II. Principal Parameters

A. Shape Parameters and Dielectric Constant

Raindrops are subjected to a number of influences: pressure, hydrodynamic stresses, surface tension, gravitational and electrical forces. These are the forces that shape a raindrop. In an early attempt to characterize the raindrop shape parameters, [6] used a sort of hydrostatic model to characterize the drops while assuming the oblate spheroid shape. The parameters of interest are the semimajor (a) and semiminor (b) axis and their ratio b/a expressed as a function of the spherical equivalent diameter D in millimeters. The possible oscillations are neglected at this stage.

Empirically, [7] suggested a polynomial to fit their measurements of b/a and those by other authors in the range of $1 \leq D \leq 7$ mm:

$$\frac{b}{a} = c_0 + c_1\, D + c_2\, D^2 + c_3\, D^3 + c_4\, D^4 \tag{1}$$

where $c_0 = 1.0048$, $c_1 = 5.7 \times 10^{-4}$, $c_2 = -2.628 \times 10^{-2}$, $c_3 = 3.682 \times 10^{-3}$ and $c_4 = -1.677 \times 10^{-4}$. Clearly, the backscatter of a radar wave with an arbitrarily oriented linear polarization will suffer a change in polarization, i.e., decomposing in horizontal and orthogonal polarization each component will be scattered differently. A parameter used to characterize the electric field inside the drop taking into account the geometry is the *depolarizing factor* ξ, which as a function of eccentricity e is

$$\xi = \frac{1}{e^2}\left(1 - \frac{b}{a}\frac{\sin^{-1} e}{e}\right) \tag{2}$$

where $e = \sqrt{1 - (\frac{b}{a})^2}$.

With the oblate shape comes different backscatter cross sections according to the wave polarization orientation. Besides, the cross section is also a function of the size and the wavelength λ. In the so called Rayleigh approximation ($\lambda \gg D$), the backscattering cross section for horizontal and vertical orientations σ_B^h and σ_B^v respectively are given by [8]

$$\sigma_B^h = \frac{\pi^5 D^6}{9\lambda^4} |f_h(D, \epsilon_r)|^2 \tag{3}$$

$$\sigma_B^v = \frac{\pi^5 D^6}{9\lambda^4} |f_v(D, \epsilon_r)|^2 \tag{4}$$

f_h and f_v are functions of geometry and dielectric properties of the drop. λ is measured in millimeters and ϵ_r is the relative complex dielectric constant of liquid water which is a function of λ and temperature T. These functions can be expressed as

$$f_h(D, \epsilon_r) = \frac{\epsilon_r - 1}{1 + \xi'(\epsilon_r - 1)} \tag{5}$$

$$f_v(D, \epsilon_r) = \frac{\epsilon_r - 1}{1 + \xi(\epsilon_r - 1)} \tag{6}$$

where $\xi' = (1 - \xi)/2$. To lend credibility to (5) and (6), note that (3) and (4) turn into the backscatter cross section of a sphere when $\xi = \xi' = \xi_{\text{sphere}}$.

B. Reflectivity Factor

The actual horizontal reflectivity η_h of a group of particles can be obtained from (3):

$$\eta_h = \int_0^{D_{\max}} \sigma_B^h \, N(D) dD \tag{7}$$

where $N(D)$ is the drop size distribution (DSD) which we will represent with a gamma distribution $N(D)dD = N_0 \, D^\mu \, e^{-\Lambda D} dD$ in the interval $(0 < D < D_{\max})$ with $D_{\max}$ =7 mm (see e.g., [2]). From the actual reflectivity, the reflectivity factor Z_h can be written as

$$\eta_h = \frac{\pi^5}{9\lambda^4} \underbrace{\int_0^{D_{\max}} D^6 N(D) |f_h(D, \epsilon_r)|^2 dD}_{Z_h} \tag{8}$$

$$Z_h = \int_0^{D_{\max}} D^6 N(D) |f_h(D, \epsilon_r)|^2 dD \tag{9}$$

in mm^6/m^3. Unlike spheres, for which the reflectivity factor is purely geometric, nonspherical particles Z_h combine geometry with dielectric properties through f_h.

C. Precipitation Estimation

The precipitation rate can be expressed in terms of $N(D)$ and the drops terminal velocity $v(D)$ as the volumetric flux of water falling to the surface

$$R = 6\pi \times 10^{-4} \int_0^{D_{\max}} D^3 \, v(D) \, N(D) \, dD \tag{10}$$

in mm/h. According to [9] $v(D) = 3.778 \, D^{0.67}$ (m/s) so R becomes a moment of the size distribution.

Clearly, R is a relative of Z_h but it is also a relative of the polarimetric variables ZDR and of KDP, therefore ,R, as mentioned above, can be written in terms of all these parameters through empirical relations.

D. Specific Attenuation

Polarimetric radars share the atmosphere as the propagation medium with many other communication systems. There is an inevitable attenuation associated with the air constituents, although the attenuation work both ways since the return *message* from the target is also attenuated. The atmospheric attenuation can be traced to a couple of very different mechanisms: 1) the scattering by particles, the 2) absorption by the same particles, and 3) the absorption by gases. The first diminishes the energy of the radar beam by redirecting it in other directions, the second decreases the energy of the beam by converting it into heat (dielectric heating in the particles), and the third by molecular excitation of gases, re-emission in other frequencies and directions and also heat.

The scattering attenuation depends strongly on the ratio between the size of the suspended particles and the wavelength. Particles of any size produce scattering but aerosols with sizes less than 1 μm (and, scattering by air molecules), can be neglected for C-band radars as compared with clouds and rain particles scattering. In addition, [10] suggests it is possible to neglect scattering by droplets smaller than 30 μm.

Moving to the absorption by gases, only O_2 and water vapor are significant at C-band frequencies [11].

Denoting as a_s and a_a the scattering and absorption specific attenuation coefficients (in 1/km), the extinction correction factor, A, can be calculated by integrating them along the path s. Another way to calculate A is to decompose a_s and a_a in contributors and then integrate:

$$A(r) = \exp\left[\int_0^r (a_g + a_c + a_p) \, ds\right] \tag{11}$$

where a_g, a_c, and a_p denote the specific attenuation by gases, clouds and precipitation respectively and r is the radar range to the target. To estimate the gas component of (11) the widely used data base HITRAN (high resolution transmission) allows a technique called *line by line* [12]. In turn, for the absorption by clouds droplets a_c the liquid water concentration as well as temperature and frequency must be taken into account. Finally, for the precipitation particles specific attenuation, a_p, the size distribution is of paramount importance.

E. Radar and Disdrometer Data

The area of interest was covered by a C-band radar located at Oro Verde, province of Entre Rios, Argentina (31.8484S, 60.53723 W). It is a polarimetric radar working at $\nu = 5.65$ GHz with 1° at 3 dB beamwidth and a peak power of 250 KW made by AMS - Gematronik GmbH. The radar data were gathered in the form of PPIs scans with a range of 240 km and a gate length of 500 m, giving 480 gates per beam and 360 beams per scan.

The elevation angles were 0.5, 1.3, 2.3, 3.5, 5.0, 6.9, 9.1, 11.8, 15.1, and 19.2° respectively.

The laser disdrometer data comes from a Thies instrument located in the city of Diamante in the same province. It can classify hydrometeor sizes in 22 categories from 0.16 to 8 mm and 20 distinct velocities from 0.2 to 20 m/s.

III. Data Modeling

A. Reflectivity Factor and Precipitation

In this section, the DSD parameters of a gamma distribution (μ, Λ, N_0) are estimated and the reflectivity factor Z_h, the precipitation rate R, and the specific attenuation a are calculated from the gamma according to (9), (10), and (11). Once temperature and frequency are fixed $|f_h(D,\epsilon_r)|^2$ (see Section III-C) calculated from (5) has a smooth dependence on D allowing a polynomial fit such as $|f_h|^2 = \sum a_j D^j$. The degree of the polynomial will depend on the desired accuracy. In particular, polynomials of third or fourth degree were considered satisfactory in the range of tropospheric temperatures with residuals up to 10^{-3}. Introducing the polynomial into (9) and (10) and integrating, Z_h and R can be written as

$$Z_h = N_0 \sum_{j=0}^{3} a_j \frac{\gamma(\mu + j + 7, \Lambda D_{\max})}{\Lambda^{\mu + j + 7}} \tag{12}$$

$$R = 6\pi \times 10^{-4} N_0\, 3.778 \frac{\gamma(\mu + 4.67, \Lambda D_{\max})}{\Lambda^{\mu + 4.67}} \tag{13}$$

where γ is the incomplete gamma function.

B. Specific Attenuation

1) Atmospheric Attenuation: In order to calculate the absorption contribution by gases, the *line by line* technique mentioned above is used with pressure and temperature and gases concentrations along the whole path as input parameters. These parameters vary with height which is important since the radar beam crosses different atmospheric layers. For calculation purposes the atmosphere was divided in $N_L = 20$ layers of equal radial thickness up to 12 km with an air composition of 21% O_2, 78% N_2, 0.0365% CO_2, and a variable quantity of water vapor. Fig. 1 shows the procedure to obtain the absorption coefficients by the considered gases. The input data consists of N_L, the radar height (H_R), the elevation angle (θ_e), and the surface temperature (T_G). With this information the model calculates the temperature, pressure, and refraction index [13] for each of the N_L layers. From this, the path length in each layer l_j is calculated as seen in the appendix.

As long as the sum of segments is less than 240 km the algorithm performs the calculation of the main absorption coefficients, i.e., water vapor and oxygen, a_v^a and a_O^a, neglecting the other gases since their absorptions are too small at C-band frequencies (see Fig. 1).

2) Cloud Attenuation: Clouds contain droplets with size distributions variable according to the kind of cloud and to which part of a cloud is observed [14]. However, it is safe to take as mean diameter $D_m = 15$ μm for a range of clouds. As

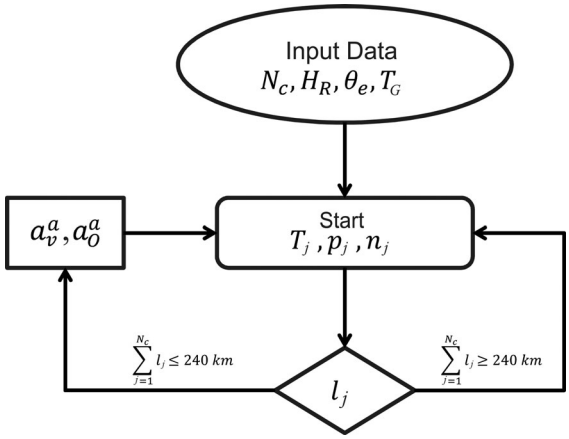

Fig. 1. Flow diagram of the algorithm used to calculate the main absorption coefficients a_v^a and a_O^a with a maximum range of 240 km.

mentioned above, the scattering of a particle is highly dependent on its size, so the attenuation by these small droplets is mainly by absorption. The process involves the complex relative dielectric constant ϵ_r and the absorbing mass, which depends on the liquid water concentration. The absorption cross section of a single droplet (σ_c^a) is given by

$$\sigma_c^a = 3\pi^2 \frac{D^3}{\lambda} \frac{\epsilon_{rI}}{(\epsilon_{rR} + 2)^2 + \epsilon_{rI}^2} \tag{14}$$

where ϵ_{rI}, ϵ_{rR} are both the imaginary and the real parts of the dielectric constant of water respectively. Following the suggestion by Pruppacher *et al.* [14] to calculate the specific absorption, the cross section (14) must be multiplied by the size distribution $N(D)\,dD = N_0/D_m\ \exp(-D/D_m)\,dD$ and integrated over sizes. N_0 and D_m are the total number of droplets per unit volume and mean diameter respectively. The resulting absorption coefficient a_c will be given by

$$a_c = 3\pi^2 N_0 3! D_m^3 1000 \frac{\epsilon_{rI}}{\lambda((\epsilon_{rR} + 2)^2 + \epsilon_{rI}^2)} \tag{15}$$

in 1/km. The cloud absorption a_c depends on ϵ_r a function of λ (fixed by the radar) and temperature which in turn takes a different value for each layer.

3) Attenuation by Precipitation: The most important absorber in a cloud is precipitation. These particles are in the millimeter range of sizes, growing at expense of the small droplets until they reach a diameter where they become unstable and break up. This diameter is about $D_{\max} \approx 7$ mm [14]. A gamma distribution of sizes [15] will be used for the calculation, but it is important to remember that since drops deform there will be a different attenuation for horizontal and vertical polarization. There will also be both absorption and scattering attenuation associated with rain.

On one hand, according to [16], the horizontal $(\sigma_{h,p}^a)$ and vertical $(\sigma_{v,p}^a)$ absorption cross sections can be expressed as

$$\begin{pmatrix} \sigma_{h,p}^a \\ \sigma_{v,p}^a \end{pmatrix} = \frac{\pi k_0}{6} D^3 \begin{pmatrix} g_h(D,\epsilon_r) \\ g_v(D,\epsilon_r) \end{pmatrix} \tag{16}$$

where,

$$\begin{pmatrix} g_h(D,\epsilon_r) \\ g_v(D,\epsilon_r) \end{pmatrix} = \frac{\epsilon_{rI}}{[1+\binom{\xi'}{\xi}(\epsilon_{rR}-1)]^2 + \binom{\xi'}{\xi}^2 \epsilon_{rI}^2} \tag{17}$$

$k_0 = 2\pi/\lambda$ is the free space wave number and ξ, ξ' are the depolarization factors defined in (5) and (6).

On the other hand, precipitation attenuation cross sections by scattering for horizontal and vertical polarization ($\sigma^s_{h,p}$) and ($\sigma^s_{v,p}$) respectively are obtained from the backscattering expressions (3) and (4) as

$$\begin{pmatrix} \sigma^s_{h,p} \\ \sigma^s_{v,p} \end{pmatrix} = \frac{2}{3}\begin{pmatrix} \sigma^h_B \\ \sigma^v_B \end{pmatrix}. \tag{18}$$

Integrating, the attenuation by absorption and scattering the coefficients are obtained

$$\begin{pmatrix} a^a_{H,p} \\ a^a_{V,p} \end{pmatrix} = N_0 \frac{\pi k_0}{6} \int_0^{D_m} D^{\mu+3} e^{-\Lambda D} \begin{pmatrix} g_h(D,\epsilon_r) \\ g_v(D,\epsilon_r) \end{pmatrix} dD. \tag{19}$$

$$\begin{pmatrix} a^s_{H,p} \\ a^s_{V,p} \end{pmatrix} = \frac{2}{3}\frac{\pi^5}{\lambda^4} N_0 \int_0^{D_m} D^{\mu+6} e^{-\Lambda D} \begin{pmatrix} |f_h(D,\epsilon_r)|^2 \\ |f_v(D,\epsilon_r)|^2 \end{pmatrix} dD. \tag{20}$$

It is observed that functions f_h, f_v, g_h, and g_v are amenable to polynomial fitting, as follows:

$$\begin{pmatrix} a^s_{H,p} \\ a^s_{V,p} \end{pmatrix} = \frac{2}{3}\frac{\pi^5}{\lambda^4} N_0 \sum_{j=0}^{4} \begin{pmatrix} a_j \\ b_j \end{pmatrix} \begin{pmatrix} \dfrac{\gamma(\mu+k+6,\Lambda D_m)}{\Lambda^{\mu+j+6}} \\ \dfrac{\gamma(\mu+j+7,\Lambda D_m)}{\Lambda^{\mu+j+7}} \end{pmatrix} \tag{21}$$

$$\begin{pmatrix} a^a_{H,p} \\ a^a_{V,p} \end{pmatrix} = N_0 \frac{\pi k_0}{6} \sum_{j=0}^{4} \begin{pmatrix} c_j \\ d_j \end{pmatrix} \begin{pmatrix} \dfrac{\gamma(\mu+j+2,\Lambda D_m)}{\Lambda^{\mu+j+2}} \\ \dfrac{\gamma(\mu+j+4,\Lambda D_m)}{\Lambda^{\mu+j+4}} \end{pmatrix} \tag{22}$$

where a_j, b_j, c_j, and d_j are the coefficients of the polynomial approximation in D, the spherical equivalent diameter.

C. Attenuation Correction Algorithm for Rain (ACAR)

Clearly, the parameters of the DSD gamma distribution are essential for the determination of attenuation as well as rainfall estimation [16]. To explain the procedure, a flow diagram is presented in Fig. 2. The input parameters: N_L, the height of the radar above the ground, H_R, the scan elevation angle, θ_e, the surface temperature, T_G and the reflectivity factor are entered in the first stage.

After entering the initial variables two subroutines are run: **Data_radar** and **Cor_Atm**. The former reads the .vol files and structures them as arrays of 480 gates in range by 360° in azimuth. The latter subroutine calculates l_j (see Appendix) and T_j for each layer and provides the absorption coefficients for **Cor_Attenuation**.

The arrays are then fed to the **gate_assignment** procedure, which determines the distribution of the 480 gates ray by ray along the atmospheric layers. This routine provides another essential parameter: the temperature T_k. Next, the subroutine

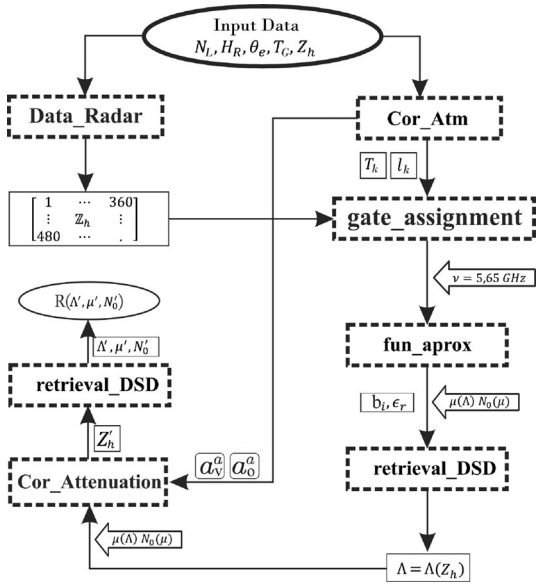

Fig. 2. Flow diagram for the ACAR algorithm.

fun_aprox uses temperature T_k and frequency $\nu = 5.65$ GHz to approximate function f_h in the interval $0.1 \leq D \leq 7$ millimeters, according to (5). In the same stage the dielectric constant distribution is obtained from [17], to calculate the coefficients b_k necessary to the procedure **retrieval_DSD**. From these relations and using (12), a function $Z_h = Z_h(\Lambda)$ can be written. Next the algorithm uses the reflectivity factor array Z_h obtained from **Data_radar** and inverts the relation $Z_h(\Lambda)$. Consequently, for each reflectivity factor there is a corresponding Λ and with (24) and (25), it is possible to retrieve the rest of the DSD parameters: (Λ, μ, N_0).

These parameters are input to **Cor_Attenuation** which corrects for attenuation Z_h using (21)–(22). The corrected reflectivity is used in **retrieval_DSD** to obtain the corrected DSD parameters (Λ', μ', N_0'). Finally, (13) gives the precipitation rate.

IV. Correction Algorithm

In (11), the contributions from gases, cloud, and precipitation are added in the exponent to calculate the attenuation. Since the radar data have been corrected by the $1/r^2$, the present algorithm only needs to correct for attenuation, beam by beam, in polar spherical coordinates. Let's call $Q(r)$ the energy flux in the beam which varies along the range due to attenuation. In discrete form, let's call Q_j the value at gate j, and if there is absorbing material between gates j and $j+1$, Q_{j+1} (and at the successive gates) will be given by:

$$Q_{j+n} = Q_{j+(n-1)} \exp\left(-2\sum A_{j+(n-1)}(\Delta r)\right)$$

where A_j is the total attenuation correction factor at gate j and $\Delta r = (r_{j+n} - r_{j+(n-1)})$ is the length of the gate (in our case $\Delta r = 0.5$ km). The factor of 2 takes into account the fact that the radiation is attenuated both ways. Another way to put the

energy flow at any gate is

$$Q_j = Q_1 \prod_{i=1}^{j-1} \exp\left(-2 \sum A_i \Delta r\right) \tag{23}$$

In the next section, we will present ACAR, an algorithm for attenuation correction that takes into account only liquid hydrometeors at this stage. This is the reason why it will be used for regions of the cloud with $Z_h \leq 55$ dBZ considering that above this figure, hail is quite likely to occur. Since ice absorption is several orders of magnitude lower than water absorption, only precipitation absorption is given a threshold. In contrast, expression (18), guarantees that given the existence of backscatter there will be attenuation irrespective of the material.

A. Precipitation Estimation Methods

The end product of interest is precipitation which is calculated after the attenuation correction by means of (13) and two algorithms by [5] using a Marshall & Palmer like equation $R(Z) = 0.017 \times 10^{0.071\,Z}$ and a R-KDP relation given by $R(K_{\rm DP}) = 40.5\,|K_{\rm DP}|^{0.85}$. In these expressions R is in mm/hr, Z in dBZ, and $K_{\rm DP}$ in degrees per kilometer. The attenuation correction is applied only to the reflectivity factor.

V. Results

Two models of attenuation, appropriate for C-band radars, are used in this work. The first (ACAR), developed in [16] and the second developed in [5] using polarimetric variables. Two volumes from the Oro Verde (INTA Parana) radar of a storm occurred on 18th of November 2009 at 03:50:03 A.M. and at 06:20:02 A.M. UTC were analyzed. For convenience only the lowest elevation was considered ($\theta_e = 0.5°$). Fig. 3 shows both storms.

Before applying any attenuation correction a number of checks had to be made to ensure the data quality. As any polarimetric radar, the INTA Parana can suffer from a series of typical problems, such as mismatched H and V channels. First, a relatively constant phase difference between the two channels of about 140° could be appreciated in the image over a large area. The most logical explanation was a phase mismatch between channels. Also, there was a mismatch in gain between both channels giving an offset of 1 dB approximately. Both anomalies were addressed by an algorithm implemented in Python within the PY/ART library based on the work by [18]. After being corrected, ZDR was useful in the identification of hydrometeors. Another important aspect to take into account when comparing radar data with ground data is that the meteorological stations must be made to coincide with a given gate within a radar beam. However, a 1 km shift in the radar position was found between the position reported by the radar itself (in the .vol file) and the actual position of the radar. More specifically the .vol files reported 31.858334S, 60.539722W, but the true location was found to be 31.848485S, 60.537233W. Consequently, the stations were inaccurately positioned from the radar.

The calculations of attenuation by the ACAR algorithm and the algorithm in [5] are applied next.

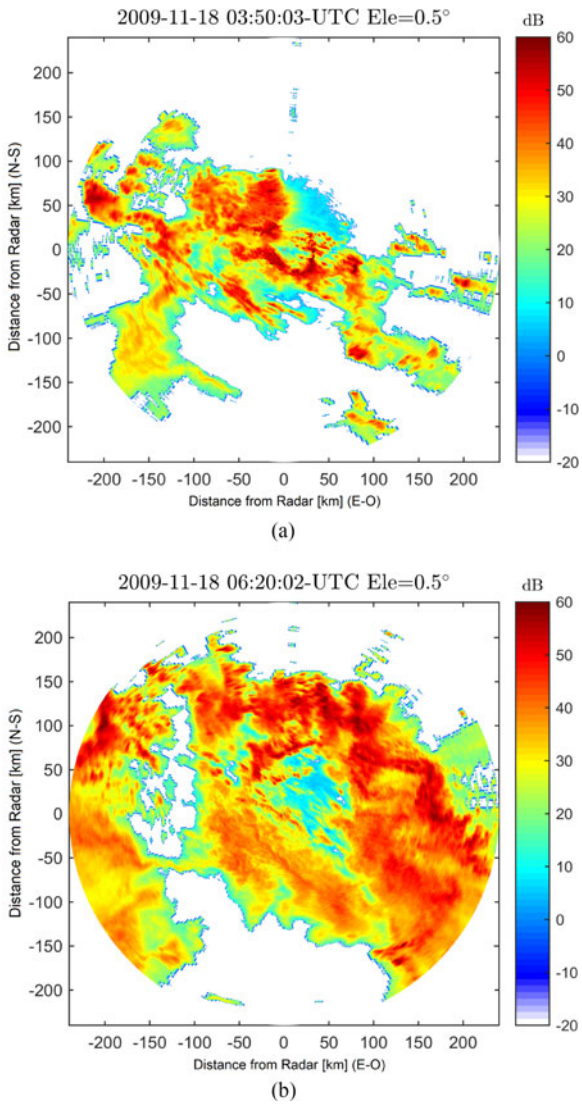

Fig. 3. Storms, in the vicinity of Oro Verde, Entre Ríos Province, used in the analysis. Top panel, PPI at 0.5 $t = 03:50$ A.M. UTC and bottom panel, PPI at 0.5 $t = 06:20$ A.M. UTC. (a) Storm 03:50:03 UTC. (b) Storm 06:20:02 UTC.

A. Attenuation Algorithm ACAR

ACAR algorithm in [16] takes into account the three attenuation processes. The initial values entered are: $N_L = 20$, $\theta_e = 0.5°$ and $T_G = 23°$ C.

1) Atmospheric Attenuation: Fig. 4 shows the frequency dependence of the absorption by O_2 and by water vapor at two temperatures 0°C and 20°C. In our case, the absorption is calculated at $\nu \approx 5.65$ GHz taking into consideration the concentration of these two gases. Clearly, at this frequency, the oxygen is the dominant factor with $a_O^a = 6.8 \times 10^{-3}$ 1/km.

2) Cloud Attenuation: The cloud attenuation calculation is carried out using (15) with N_0 calculated by expressing the liquid water concentration in a progression from the lower to the higher reflectivities and keeping the mean diameter fixed at $D_m = 15$ μm on the whole radar range but under the condition $Z_h^{\rm INTA} > 1$ dBZ so as to make sure the existence of cloud material. Fig. 5 shows how the correction factor for the storm

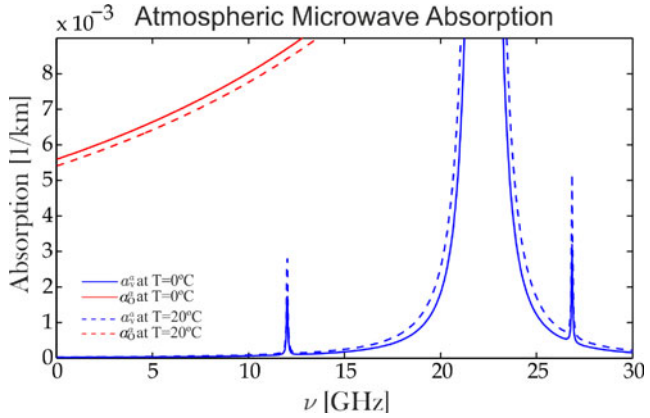

Fig. 4. Absorption coefficients of oxygen a_o^a and water vapor a_v^a in red and blue, respectively, for $T = 0\,^{\circ}\mathrm{C}$ and $20\,^{\circ}\mathrm{C}$.

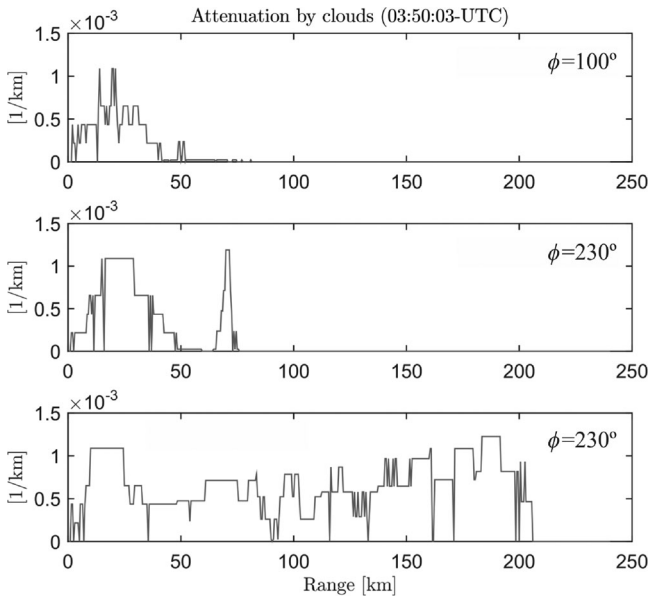

Fig. 5. Coefficient a_c for three azimuths.

at 03:50 A.M. follows the variations in N_0. Three azimuths are shown in Fig. 5 to verify the correct behavior of the algorithm. As seen in this figure, the attenuation is under 10^{-3} 1/km.

3) DSD Retrieval From Disdrometer: The ACAR algorithm needs the gamma DSD parameters (μ, Λ, N_0) and their mutual relationships [19]. The disdrometer at Diamante City provides the data to build the DSDs and from which the parameters and their relations are extracted (see, [20]). Fig. 6 shows how these parameters depend on each other:

$$\mu = -0.02979\,\Lambda^2 + 1.242\,\Lambda - 1.374 \tag{24}$$

$$N_0 = \exp(0.035\,\mu^2 + 0.54\,\mu + 7.13). \tag{25}$$

4) Results of Attenuation by Precipitation: Once the relations (24) and (25) are obtained, they are replaced in (22) and (21) to get the coefficients needed in (23). Fig. 7 shows the coefficient for the storm at 03:50 A.M. in the direction of azimuth 201°. The upper part shows the contributions by absorption (blue) and scattering (red) to the attenuation of a horizontal polarized beam. Bottom panels show that at certain ranges, where the upper limit in Z_h has been reached, absorption is put to zero while the scattering is still active, as has been explained at the end of Section IV. Clearly, the dominant factor in attenuation is absorption, which is dependent on the concentration of liquid water and drop size while scattering depends strongly on size. Fig. 8 corresponding to the storm at 06:20 A.M. supports this

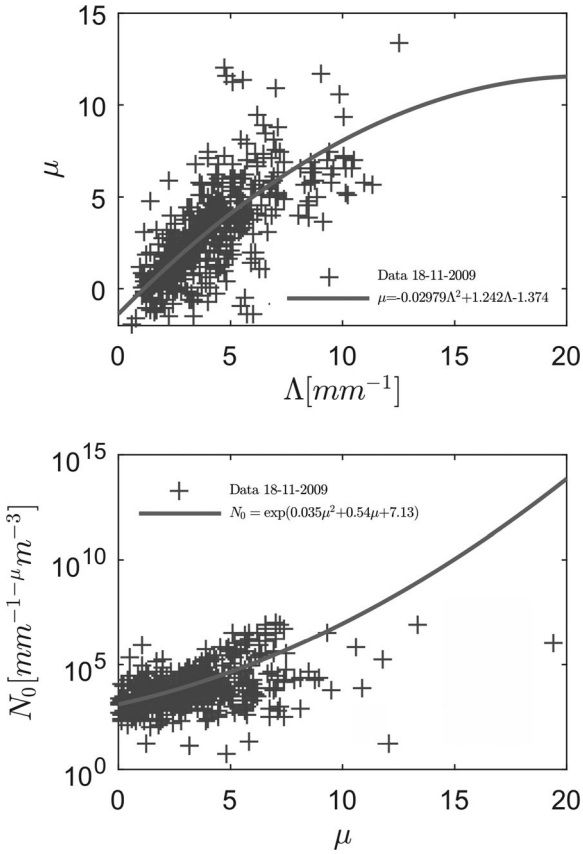

Fig. 6. Relationships between pairs of DSD parameters obtained from disdrometer during November 18th, 2009.

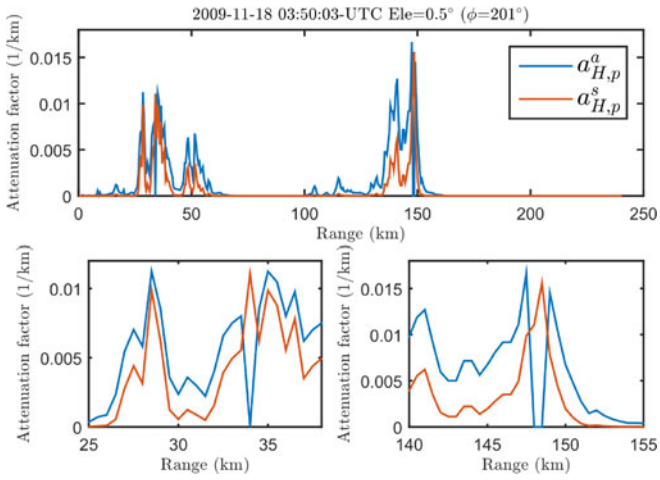

Fig. 7. Attenuation factor for horizontal polarization absorption $a_{H,p}^a$ and scattering $a_{H,p}^s$ for the beam at $\phi = 145^{\circ}$ azimuth calculated using ACAR for the storm at 03:50 A.M.

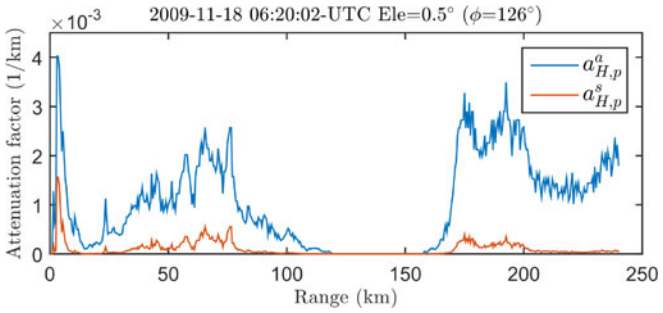

Fig. 8. Attenuation factor for horizontal polarization absorption $a^a_{H,p}$ and scattering $a^s_{H,p}$ for azimuth $\phi = 126°$ obtained from ACAR at 06:20 A.M.

observation. Actually, in both figures Figs. 7 and 8, the absorption attenuation is larger than scattering attenuation of a polarized wave.

Finally, it is necessary to apply the just calculated attenuation correction factor.

5) Comparison of ACAR With Gu et al. algorithm: To give an independent assessment of ACAR performance, another known algorithm from the literature [5] was used. Fig. 9(a) for the storm at 03:50 A.M. shows this comparison for three azimuths with various reflectivity intensities. In the top plot (Az. 45^o) with low reflectivity, both correction factors are negligible. The middle plot for Az. 225^o shows that the uncorrected reflectivity at 240 km range is 24.5 dBZ and the Z_h corrected by Gu *et al.* [5] is 32.51 dBZ and by Poffo [16] is 28.26 dBZ. Similarly, the lower plot for Az. 345^o at a range of 90 km, the uncorrected value is $Z_h = 41.5$ dBZ and corrected values are 45.61 dBZ and 45.48 dBZ for [5] and [16], respectively.

Similar comparisons are made for the storm at 06:20 A.M. and shown in Fig. 9(b). There are some differences to be noted. In the middle plot (Az. 114^o) the correction begins around 100 km, although it is more important beyond the echo of about 50 dBZ, and both models give similar values but with [16] the correction increases. This fact contrasts with the middle plot on Fig. 9(a). Nevertheless, the latter shows echoes above 55 dBZ for which ACAR does not apply the contribution of precipitation absorption to the attenuation. This effect is also noticed at the bottom of Fig. 9(a) after crossing 55 dBZ. In general, as long as echoes do not go over 55 dBZ, ACAR produces a larger attenuation correction. Fig. 10 shows the effect of the corrections on the images. Top panels represent the original images for both storms. The middle panel shows the image corrected by ACAR and in the lower two panels the corrections by Gu *et al.* [5]. In the latter, note a missing area at about (50 km,50 km) due to the low $\rho_{\rm hv}$ which is considered noise by [5]. In order to show where one correction prevails over the other, image subtraction are presented in Fig. 11 The lower panel shows the difference before-after the ACAR correction. The difference is calculated in mm^6/m^3 and then converted to dBZ. The correspondence between large correction magnitudes and reflectivity factor in Fig. 3 can be noticed. This difference should be contrasted with that illustrated in Fig. 8, which is quite smaller because it corresponds to the ratio of two magnitudes close to each other in value . In the upper panel of

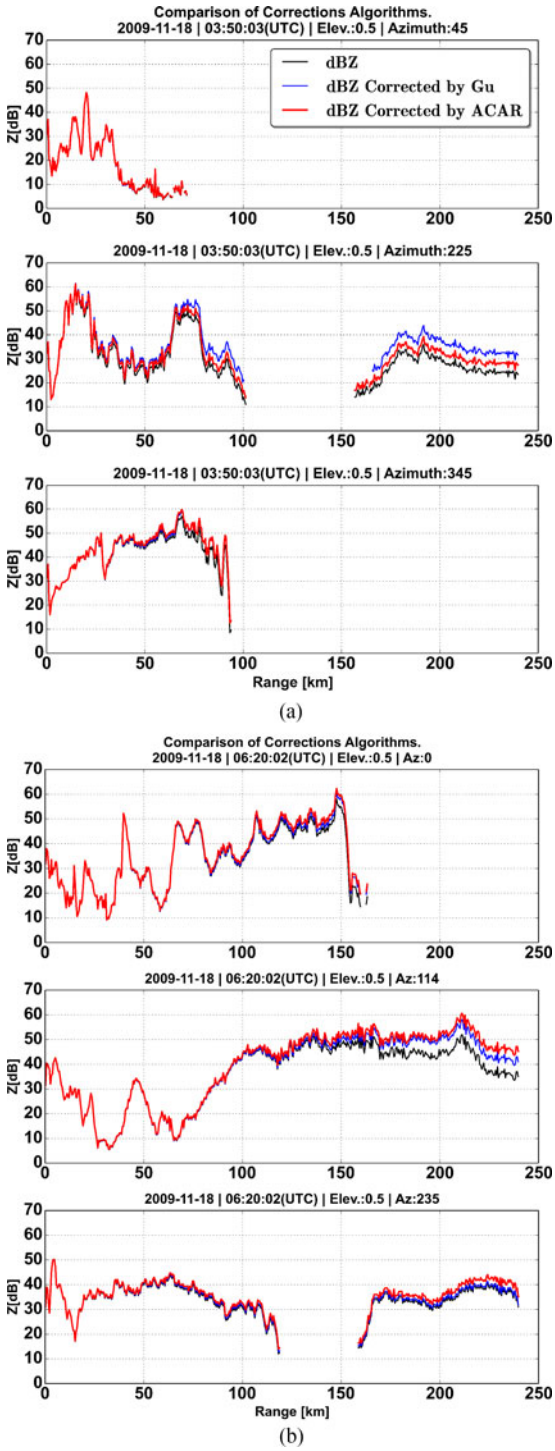

Fig. 9. Reflectivity factor along a ray for three azimuths: Uncorrected (black), ACAR (red) and [5] (blue) Corrected. (a) Storm 03:50:03 UTC. (b) Storm 06:20:02 UTC.

Fig. 11, the difference in mm^6/m^3 between the image corrected by ACAR, and that corrected by Gu *et al.* [5] is calculated using the following procedure. First, the differences smaller than 1 mm^6/m^3 are filtered out. Next the dBZ of the absolute value of the difference is calculated and multiplied by the sign function of the difference. Therefore, the positive values represent zones where ACAR dominates and viceversa. It is clear that

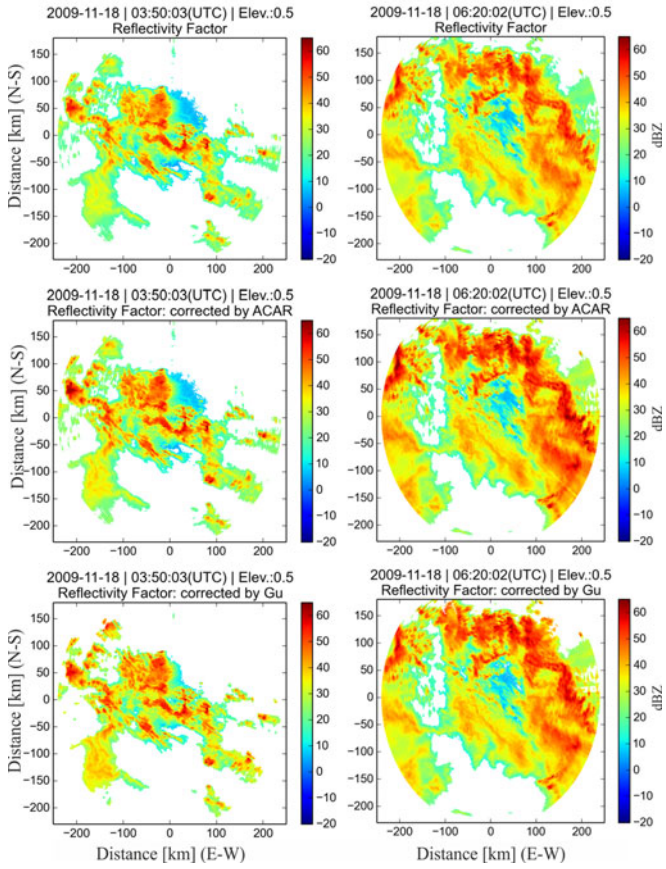

Fig. 10. Two analyzed storms. Left at 03:50 hrs and right at 06:20 hrs. Top pair of panels, uncorrected images. Middle, the ACAR correction and bottom pair, the correction by Gu *et al.* [5].

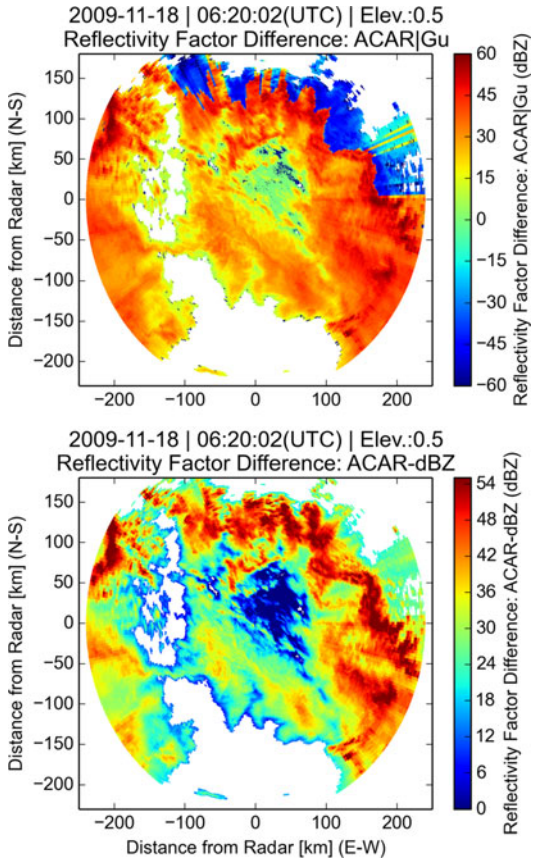

Fig. 11. Correction amount for ACAR (lower panel) and difference between corrections by ACAR and [5] (upper panel). The differences are performed in linear scale and then converted to dBZ.

ACAR corrects over [5] in most part of the scan. However, there is a region over the NNE sector in which the converse occurs probably due to the presence of hail, as explained above. The only way to find out which attenuation correction is more adequate is to evaluate the precipitation after applying the correction, and then compare the predicted rainfall with rain gauges on the ground. For this purpose, four stations with rain gauges (one with disdrometer) were used. The location of the stations relative to the radar can be seen in Fig. 12. Their position in geographical coordinates are: Parana (31.728180S, 60.528058W), Diamante (32.066667S, 60.65W), Villa Urquiza (31.652777S, 60.368611W), and Villaguay (31.8575S, 59.09722W). Table I shows azimuth and range from the radar of each station together with the radar gate above the rain gauge and the time the radar beam passes over the station. All these stations are automatic and record every 10 or 30 min. Once this data are averaged in time they are compared with the storms at 03:50 A.M. and 06:20 A.M. The top row of Fig. 13, shows comparisons for the storm at 03:50 A.M. and on the bottom row comparisons for the storm at 06:20 A.M. Each group of bars represents a station location and the leftmost bar of the group is the rain gauge or disdrometer measurement (seen in Table I), and the other bars are the results of the estimation algorithms. Next to the right is the estimation by ACAR (10) and by Gu *et al.* [5]. The other methods explained at the beginning of Section IV-A are also

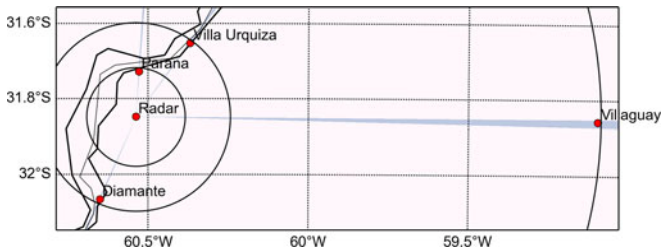

Fig. 12. Ground stations with rain gauges used to compare with the precipitation estimation.

TABLE I
RAIN GAUGE DATA

Stations rain gauge	Range (m)	Gate	Azimuth(°)	Beam time of arrival (s)
Parana	13 250	26	4	3.38
Diamante	26 750	53	204	14.5
Villa Urquiza	27 250	54	36	5.165
Villaguay	136 250	272	91	8

used for comparison: $R_{Z-\mathrm{ACAR}}$, R_{KDP} and are represented by the last two bars. In general, all algorithms tend to overestimate the rain rate and the present model (denoted by R_{ACAR} in the graph) behaves better than others specially for Diamante. There are a couple of extreme cases to note: panels (c) and (d). The former with essentially zero measured precipitation and all

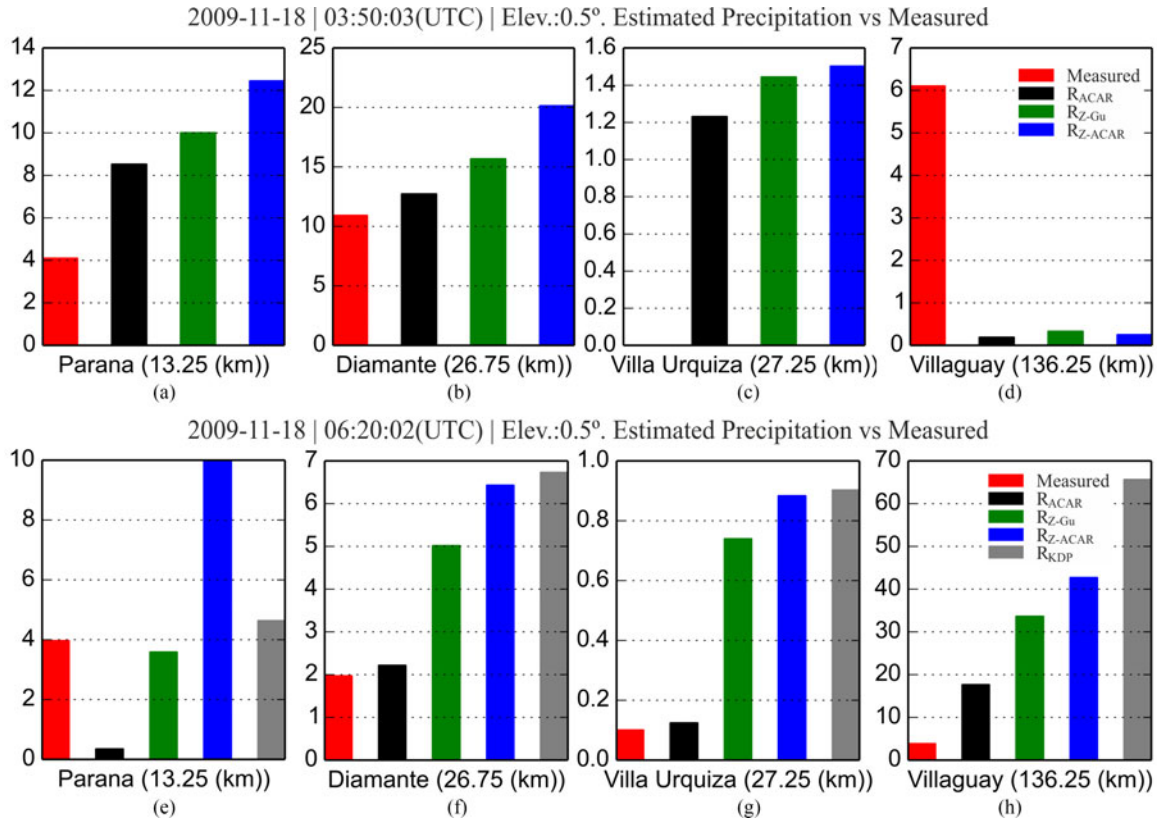

Fig. 13. Comparison between rain gauges and precipitation estimation from data corrected for attenuation. From left to right: measured, R from $ACAR$, R from [5], R from M-P using ACAR and R_{KDP}.

algorithms predicting light rain, and the latter where the rain gauge measured a sizable rain and all algorithms predicted almost no precipitation. About this last case, there are a couple of arguments to take into consideration. First, there were scatter showers in the area of Villaguay. Second, the distance (136 km) is far enough to observe higher in the cloud and taking the wind into account the coincidence echo-rain gauge could be lost. In fact, neighboring gates have larger reflectivities which support this hypothesis. Another aspect to consider is the larger resolution volume at long range that may contribute to the underestimation in the Villaguay case at 03:50 A.M. The opposite occurs at 06:20 A.M. At that location the beam is almost filled up but the rain gauge is in a lower intensity point (see bottom panel of Fig. 3 and all the algorithms apparently overestimate.

VI. Conclusion

The algorithm ACAR was presented and used to correct radar data for attenuation. It uses both, effects of atmospheric gases as well as those of microphysical parameters. By means of this model, oxygen was confirmed as the most absorbing gas at $\nu =$ 5.65 GHz with an attenuation of around $a_O^a = 6.8 \times 10^{-3}$ 1/km and the cloud droplets attenuation was calculated as relatively weak, with factors of less than 10^{-3} 1/km.

As far as precipitation attenuation is concerned, to write (22) and (21) the DSD must be known. The disdrometer in Diamante station provided the data to obtain the DSD and the relations $\Lambda - \mu$ and $N_0 - \mu$ at that location. Interestingly, these relations were very similar to those of [9]. However, there is a different independent term in the relation $N_0 - \mu$ when fitted by a polynomial. This has important consequences because the independent term gives rise to the initial number concentration of raindrops. As mentioned above when the Z_h goes over 55 dBZ absorption in ACAR model is put to zero because of the probable existence of ice, as hail, which has very low absorption. Scattering continues to operate even in this situation, see Fig. 7. A possible complication arises when hail begins to melt as it falls and has a layer of liquid water on top. This would enhance both absorption and scattering. It is not surprising that the comparison of ACAR with [5] and attenuation models implemented in the CSU-PY-ART library were good as long as $Z_h < 55$ dBZ and above this value, corrections are different. Undoubtedly, a better characterization of the nature of the hydrometeors in the ACAR model will be of great help.

Unfortunately, the use of ground data from four stations were inconclusive to determine which correction model was the best. This results shows that instantaneous comparisons are not reliable. In conclusion, the statistical nature of the precipitation process shows that longer averages will be necessary to throw light into this matter.

Appendix A
Radar Beam Path in a Layered Atmosphere

For an atmosphere with discrete layers Snell's law can be applied at each interface. Fig. A.1 shows the beam trajectory

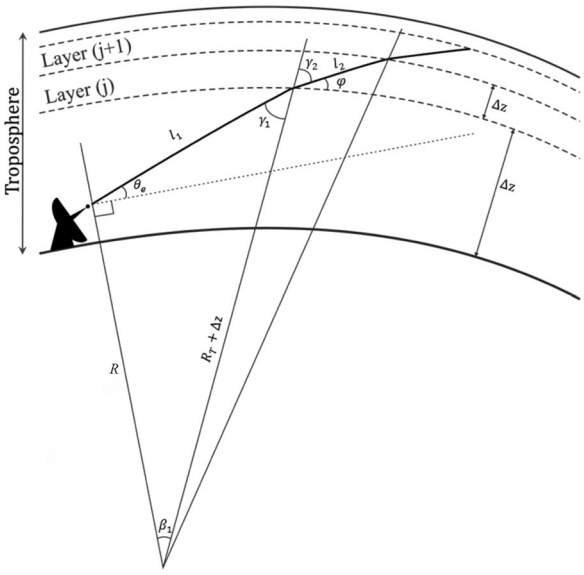

Fig. A.1. Geometry for the beam propagation in a layered atmosphere used in ACAR model.

geometry and the triangles on which trigonometric relations can be applied.

In order to calculate the segment l_1, the cosine theorem is applied on the first triangle

$$(R + \Delta z)^2 = l_1^2 + R^2 - 2\, l_1\, R\, \cos(90 + \theta_e) \tag{A.1}$$

where $R = (R_T + H_R)$ is the Earth radius plus the radar height, Δz is the thickness of the layers (taken uniform) and θ_e is the radar elevation angle.

Solving the quadratic equation for l_1, taking the positive sign for the square root and rearranging terms yields:

$$l_1 = -R\, \sin(\theta_e) + ((R\, \sin(\theta_e))^2 + \Delta z\, (2\, R - \Delta z))^{1/2}. \tag{A.2}$$

For the next segment it is necessary to calculate φ. The sin theorem gives

$$\sin(\gamma_1) = \cos(\theta_e) \frac{R}{R + \Delta z}. \tag{A.3}$$

Now, applying Snell's law relating γ_1 and γ_2 and since $\varphi = \pi/2 - \gamma_2$

$$\varphi = \arccos\left(\frac{n_1 R \cos(\theta_e)}{n_2 (R + \Delta z)}\right). \tag{A.4}$$

Applying the same procedure used for l_1 to l_2

$$\begin{aligned} l_2 = & -(R + \Delta z)\, \sin(\varphi) + ((R + \Delta z)\, \sin(\varphi))^2 \\ & + \Delta z\, (2\, R + \Delta z))^{1/2}. \end{aligned} \tag{A.5}$$

The successive application of the procedure leads to the general expression for the j-layer ($j > 1$):

$$\begin{aligned} l_j = & -(R + (j-1)\Delta z)\alpha_j + ((R + (j-1)\Delta z)^2\, \alpha_j^2 \\ & + \Delta z(2R + (2j-3)\Delta z))^{1/2} \end{aligned} \tag{A.6}$$

where

$$\alpha_j = \sin\left[\arccos\left(\frac{R\, n_1\, \cos(\theta_e)}{(R + (j-1)\Delta z)\, n_j}\right)\right]. \tag{A.7}$$

Here n_j denotes the refraction index of the j-layer. The refraction index depends on temperature T_j in each layer, which is calculated using the standard atmosphere lapse rate (6.5 K/km).

ACKNOWLEDGMENT

The authors would like to thank to Dr. P. Salio (FCEyN - University of Buenos Aires) for providing radar and disdrometer data.

REFERENCES

[1] J. S. Marshall and W. M. K. Palmer, "The distribution of raindrops with size," *J. Meteorology*, vol. 5, no. 4, pp. 165–166, 1948.
[2] C. W. Ulbrich and D. Atlas, "Rainfall microphysics and radar properties: Analysis methods for drop size spectra," *J. Appl. Meteorology*, vol. 37, no. 9, pp. 912–923, 1998.
[3] V. Bringi and V. Chandrasekar, *Polarimetric Doppler Weather Radar: Principles and Applications*. Cambridge, U.K.: Cambridge Univ. Press, 2001.
[4] A. V. Ryzhkov, S. E. Giangrande, and T. J. Schuur, "Rainfall estimation with a polarimetric prototype of wsr-88d," *J. Appl. Meteorology*, vol. 44, no. 4, pp. 502–515, 2005.
[5] J.-Y. Gu *et al.*, "Polarimetric attenuation correction in heavy rain at c band," *J. Appl. Meteorology Climatology*, vol. 50, no. 1, pp. 39–58, 2011.
[6] A. Green, "An approximation for the shapes of large raindrops," *J. Appl. Meteorology*, vol. 14, no. 8, pp. 1578–1583, 1975.
[7] K. V. Beard and C. Chuang, "A new model for the equilibrium shape of raindrops," *J. Atmospheric Scie.*, vol. 44, no. 11, pp. 1509–1524, 1987.
[8] R. J. Hogan, L. Tian, P. R. Brown, C. D. Westbrook, A. J. Heymsfield, and J. D. Eastment, "Radar scattering from ice aggregates using the horizontally aligned oblate spheroid approximation," *J. Appl. Meteorology Climatology*, vol. 51, no. 3, pp. 655–671, 2012.
[9] G. Zhang, J. Vivekanandan, and E. Brandes, "A method for estimating rain rate and drop size distribution from polarimetric radar measurements," *IEEE Trans. Geosci. Remote Sens.*, vol. 39, no. 4, pp. 830–841, Apr. 2001.
[10] J. P. Burrows, U. Platt, and P. Borrell, *Tropospheric Remote Sensing From Space*. New York, NY, USA: Springer, 2011.
[11] A. Papatsoris and P. Watson, "Calculation of absorption and dispersion spectra of atmospheric gases: At millimetre-wavelengths," *IEE Proc. Microw., Antennas Propag. H*, vol. 140, no. 6, pp. 461–468, Dec. 1993.
[12] L. Rothman *et al.*, "The hitran2012 molecular spectroscopic database," *J. Quantitative Spectroscopy Radiative Transfer*, vol. 130, pp. 4–50, 2013.
[13] R. J. Doviak and D. S. Zrnic, *Doppler Radar & Weather Observations*. New York, NY, USA: Academic, 2014.
[14] H. R. Pruppacher, J. D. Klett, and P. K. Wang, "Microphysics of clouds and precipitation," 1998.
[15] C. W. Ulbrich, "Natural variations in the analytical form of the raindrop size distribution," *J. Climate Appl. Meteorology*, vol. 22, no. 10, pp. 1764–1775, 1983.
[16] D. A. Poffo, "Influencia del medio atmosférico en la atenuación del haz de radar," Tesis de Especialización," *Facultad de Matemática, Astronomía y Física (UNC)*, 2014. [Online]. Available: http://www.famaf.unc.edu.ar/wp-content/uploads/2014/04/Trabajo-final-de-espe cialización-Poffo-.pdf.
[17] T. Meissner and F. J. Wentz, "The complex dielectric constant of pure and sea water from microwave satellite observations," *IEEE Trans. Geosci.Remote Sens.*, vol. 42, no. 9, pp. 1836–1849, 2004.
[18] S. E. Giangrande, R. McGraw, and L. Lei, "An application of linear programming to polarimetric radar differential phase processing," *J. Atmospheric Oceanic Technol.*, vol. 30, no. 8, pp. 1716–1729, 2013.
[19] M. Schleiss and J. Smith, "A method to estimate the 3d–time structure of the raindrop size distribution using radar and disdrometer data*," *J. Hydrometeorology*, vol. 16, no. 3, pp. 1222–1242, 2015.
[20] L. S. Kumar, Y. H. Lee, and J. T. Ong, "Shape slope parameter distribution modelling of electromagnetic scattering by rain drops," *Prog. Electromagn. Res. B*, vol. 25, pp. 191–209, 2010.

Denis Alexander Poffo was born in Buenos Aires, Argentina, 1984. He received the Licentiate degree in astronomy from Facultad de Matemática, Astronomía y Física (FaMAF), Universidad Nacional de Córdoba, Córdoba, Argentina, and the Specialist degree in radar system and instrumentation from FaMAF.

He is currently working toward the Master's degree in radar system and instrumentation in the same institution. Since 2012, he has been at FaMAF as a scholarship holder. His research interests include meteorological applications of polarimetric radar with emphasis on rainfall estimation and weather hazard detection.

Jorge Nicolás Saffe was born in San Juan, Argentina, in 1986. He received the Computer Engineer's degree from Facultad de Ciencias Exactas, Físicas y Naturales, Universidad Nacional de Córdoba, Córdoba, Argentina, in 2012.

He is currently working toward the Master's degree in radar system and instrumentation at Facultad de Matemática, Astronomía y Física (FaMAF) of the same University.

Since 2014, he has been at FaMAF as a Ph.D. scholarship holder. His research subject is the development of a multistatic system for weather radars.

Giorgio Mario Caranti was born in Monfalcone, Italy, in 1946. He received the Licentiate degree in physics from the National University of Córdoba, Argentina, in 1970 and the Ph.D. degree in physics from the University of Manchester, England, 1982.

He was a Research Assistant in Facultad de Matemática, Astronomía y Física (FaMAF), Córdoba, 1971. From 1978 to 1982, he was at Manchester with a Scholarship from The National Scientific and Technical Research Council (CONICET). Later he was an Adjunct Professor up to 1989 and a Full Professor until his retirement in 2012. He was a Researcher at CONICET from 1985 to 2012 reaching the Principal category in 2002. During 1987–1989, he was an Adjunct Associate Professor of physics in the New Mexico Institute of Mining and Technology, Socorro, NM, USA. He directed the Atmospheric Physics Laboratory of FaMAF from its creation up to 2004. He is currently supervising the Sistema Nacional de Radares Meteorolgicos (SINARAME) project of meteorological radar coverage of Argentina. His research interests include microphysics of clouds, ice physics, charge transfer, cloud electrification, lightning physics, and radar meteorology. He is the author and coauthor of more than 80 papers, more than 120 conference presentations and, one patent.

Raúl Alberto Comes received the Licentiate degree in physics from Facultad de Matemática, Astronomía y Física (FaMAF), Universidad Nacional de Córdoba, Córdoba, Argentina and the Ph.D. degree in atmospheric physics from the New Mexico Institute of Mining and Technology, Socorro, NM, USA, in 1975 and 1988, respectively.

From 1976 to 1983, he was an Assistant Researcher in the Atmospheric Physics Group of FaMAF and since 1988, he is an Adjunct Professor in the same area. He is currently participating in the Sistema Nacional de Radares Meteorolgicos (SINARAME) project of meteorological radar coverage of Argentina. His research interests include cloud physics and weather radar applications with an emphasis on radar echo interpretation.

Andres Rodriguez (M'16) was born in Córdoba, Argentina, 1961. He received the Civil Engineering degree from the National University of Cordoba, Cordoba, Argentina, 1985 and the Ph.D. degree in marine sciences from the Politechnical University of Catalonia (UPC), Barcelona, Spain, 1997.

He began his carrier as a Research Assistant at Facultad de Cs. Exactas Físicas y Naturales (FCEFyN), Córdoba, Argentina, 1981. Later he was an Adjunct Professor since 1990. Since 1997, he has been a Full Professor. He was a Researcher at The National Scientific and Technical Research Council (CONICET) from 2001 to the present reaching the Independent category in 2007. During 1991–1997, he was an Associate Professor of Maritime Hydraulics at the Laboratory of Maritime Engineering (LIM) Engineering, UPC, Barcelona, Spain. He is an Associate Researcher of National Water Institute since 1997. He is currently the Director of the Hydraulics Laboratory, FCFyN since 1997 . He was the President of Directory of Superior Institute of Water Resources ISRH of UNC since its creation in 2002 up to 2007, and the Director of the Sistema Nacional de Radares Meteorolgicos (SINARAME) project of meteorological radar coverage of Argentina since its creation in 2009 up to 2015. His research interests include fluvial hydraulics, experimental and numerical hydrodynamics, maritime and environmental engineering, and radar hidro-meteorology. He is the author and coauthor of more than 53 papers, 9 book chapters, 3 books, and more than 200 conference presentations and one patent.

Dr. Rodriguez received the national prize of National Academy of Engineering in 2000.